low incidence of acute gastrointestinal morbidity was encouraging, the reason for the high incidence of acute GU morbidity has not been fully investigated.

The proton beam can produce target nuclear reactions, a process termed *autoactivation* (7, 8). The positions and number of β^+ decayed nuclei were determined by simultaneous measurement with a positron emission tomography (PET) scanner to detect pairs of photons emitted from the positron–electron annihilation subsequent to the nuclear fragment reaction (9). Although the proton-irradiated area and the path were confirmed by PET imaging, it is unclear whether the intensity and distribution of β^+ decayed nuclei were consistent with the calculated dose distribution and whether the acquired PET images could be used to verify the proton beam therapy. We used PET images to confirm the proton-irradiated area. Although those PET images seemed to be grossly matched to the calculated doses, an unexpected distribution of β^+ decayed nuclei can occur relative to the surrounding regions. Because those distributions seemed to spread outside the planning target volume (PTV), we hypothesized that physiologic factors might have affected them. In this study we focused on the significance of urinary autoactivation after proton beam therapy in patients with prostate cancer.

METHODS AND MATERIALS

Patients

From December 2006 to July 2008, autoactivation after proton beam irradiation was investigated in 59 patients with prostate cancer. Of these, 29 underwent PET to monitor distribution-relevant autoactivation, and the remaining 30 patients were subjected to direct measurement of autoactivation in the urine. All patients had been diagnosed with histologically proven prostate cancer, with no evidence of metastasis to the pelvic lymph nodes or at distant sites, and an Eastern Cooperative Oncology Group performance status of 0, 1, or 2. Other details of the patients and tumor characteristics are presented in Table 1. This study was approved by both the Kobe University Institutional Committee (Kobe, Japan) and the Hyogo Ion Beam Medical Center Institutional Committee.

Table 1. Details of patient characteristics treated with proton therapy ($N = 59$)

Characteristic	2006–2007 ($n = 29$)	2007–2008 ($n = 30$)	p Value
Age (y)			0.16
Range	59–83	53–82	
Median	70	69	
T stage (No. of patients)			0.82
T1	7	7	
T2	18	18	
T3	4	5	
Gleason sum (No. of patients)			0.55
2–6	11	9	
7	13	14	
8–10	5	7	
PSA (No. of patients)			0.10
<10.0 ng/mL	12	15	
10.0–20.0 ng/mL	9	8	
>20.0 ng/mL	8	7	
CTV (No. of patients)			0.97
<30 cm^3	15	16	
>30 cm^3	14	14	

Abbreviations: PSA = prostate specific antigen; CTV = clinical target volume.

Proton beam therapy

The planning and treatment methods have been described previously (6). In brief, computed tomography (CT) and magnetic resonance imaging fusion with CT-based dose calculation is the routine treatment planning procedure at our institution. Doses were calculated with the pencil beam algorithm. Beam parameters, including the width of the SOBP and degrader thickness, were selected with a three-dimensional treatment-planning system (FOCUS-M; jointed CMS Japan Co. [Tokyo, Japan] and Mitsubishi Electric Corporation [Kobe, Japan]). The clinical target volume (CTV) was taken to be the prostate and the base of the seminal vesicles, as visualized on the fused CT and magnetic resonance images. The initial PTV was defined as the three-dimensional isotropic expansion of the CTV, together with a 1-cm boundary. The second PTV was defined almost identically to the initial PTV except that the posterior margin was the CTV plus 0.8 cm for the last 14 GyE in seven fractions. By including 0.5 cm around the PTV as a penumbra, the initial irradiation fields were customized with 3.75-mm-wide multileaf collimators. Certain critical surrounding structures, including the rectum, bladder, and femoral head, were also delineated on each CT slice to generate dose–volume histograms. A daily fraction dose of 2 GyE was delivered with a single port by use of the laterally opposed field technique. All patients were treated with 210-MeV protons at a dose of 74 GyE in 37 fractions over a period of 7.4 weeks.

Autoactivation imaging using clinical PET apparatus

Data acquisition for autoactivation was performed on the third or fourth day after the start of the treatment. The acquisition was started at 5 minutes after each proton irradiation by use of a clinical PET scanner (Headtome V, SET-2300 W; Shimadzu Corporation, Kyoto, Japan), and the data were analyzed with vendor-provided software. After each daily treatment, patients were immediately transferred in a wheelchair to a PET room by medical staff. At our institution, the PET room and the proton therapy unit are located near each other, in the same building. Patients were positioned on the PET scanner in the treatment position without an immobilization device. Detection of activity induced by the autoactivation commenced 5 minutes after completion of the proton beam irradiation protocol, and the data were recorded for 5 minutes. Data corrected for attenuation were acquired with a ^{68}Ge-^{68}Ga transmission source. The acquired image data were interpreted by use of the vendor-provided software. Images were fused to the three-dimensionally reconstructed CT images by use of the axial, sagittal, and coronal views. Regions of interest (ROIs) were drawn on the reconstructed image data, and activity was measured by use of two-dimensional axial images across the following 5 portions: PTV center, urinary bladder inside the PTV, urinary bladder outside the PTV, rectum (outside the PTV), and contralateral femoral bone head (outside the PTV). The calibration of activity was conducted separately in each ROI (Cylinder Phantom, 37 MBq, PET-20C19/1-SZ; Sanders Medical Products, Knoxville, TN). To elucidate direct and indirect influence of prostate gland size (was equal to CTV) on the urine autoactivation, data acquisition was performed in two groups. One group consisted of patients whose CTV was less than 30 cm^3, and the other consisted of patients whose CTV was more than 30 cm^3.

Investigation of autoactivation using water phantom

Autoactivation after proton beam irradiation was also investigated by use of a water phantom in a setting similar to that used in clinical practice. The 210-MeV proton beam's effect was compared with that of a 10-MV X-ray for this experiment. A single dose of 6 Gy was used for comparison with a water phantom or similarly sized ice block (20 × 20 × 15 cm). The proton beam was delivered to the water phantom once a day. The field size of the irradiation was 15 × 15 cm. The Bragg peak of the proton beam was spread over 6 cm, and the range of the proton beam was adjusted to 13 cm by use of a degrader. After proton beam irradiation, the water phantom or ice block was moved to the PET room immediately, as is done in clinical practice. Calculation of the activity induced by proton beam or X-ray irradiation began about 5 minutes to 60 minutes after irradiation. The ice block was used to examine whether there was any connection with water's diffusive behavior. Therefore the same volumes of water and ice were assessed. The ice block measured 20 × 20 × 15 cm, and 6,000 mL of pure water was used.

Direct measurement of autoactivation in urine

On the third or fourth day after the start of treatment, patients were quickly moved to a separate room for urination after receiving proton beam therapy, and each 2-mL urine sample was transferred to a test tube. Radioactivity of the urine was measured beginning 5 minutes after treatment until 40 minutes after treatment by use of a well counter (CRC-15 W; Capintec, Ramsey, NJ). Measurement lasted 30 seconds, and the energy window ranged from 400 to 660 keV. The setting was selected to reach energy of 511 keV for pair-annihilation photons from β^+ decaying nuclei generated by autoactivation.

Statistics

The chi-square test was performed to assess measures of association in a grouped frequency table. To compare activity in each ROI, box-and-whisker plots were used and analyzed by *t* test.

RESULTS

Comparison between calculated dose and distribution of autoactivation by PET

Since our institution started using proton beam therapy, we have used autoactivation images for confirming the proton beam path in many types of malignancies. A representative case of prostate cancer is shown in Fig. 1. Figures 1A and 1D show axial and sagittal images of the dose distribution calculated by use of the pencil beam algorithm, and Figs. 1B and 1E show the distribution of autoactivation in the upper PTV level in patients with prostate cancer receiving 2 GyE of proton beam irradiation. Figures 1C and 1F show axial and sagittal CT-PET fusion images. On the axial images, although the beam passage was well matched to the

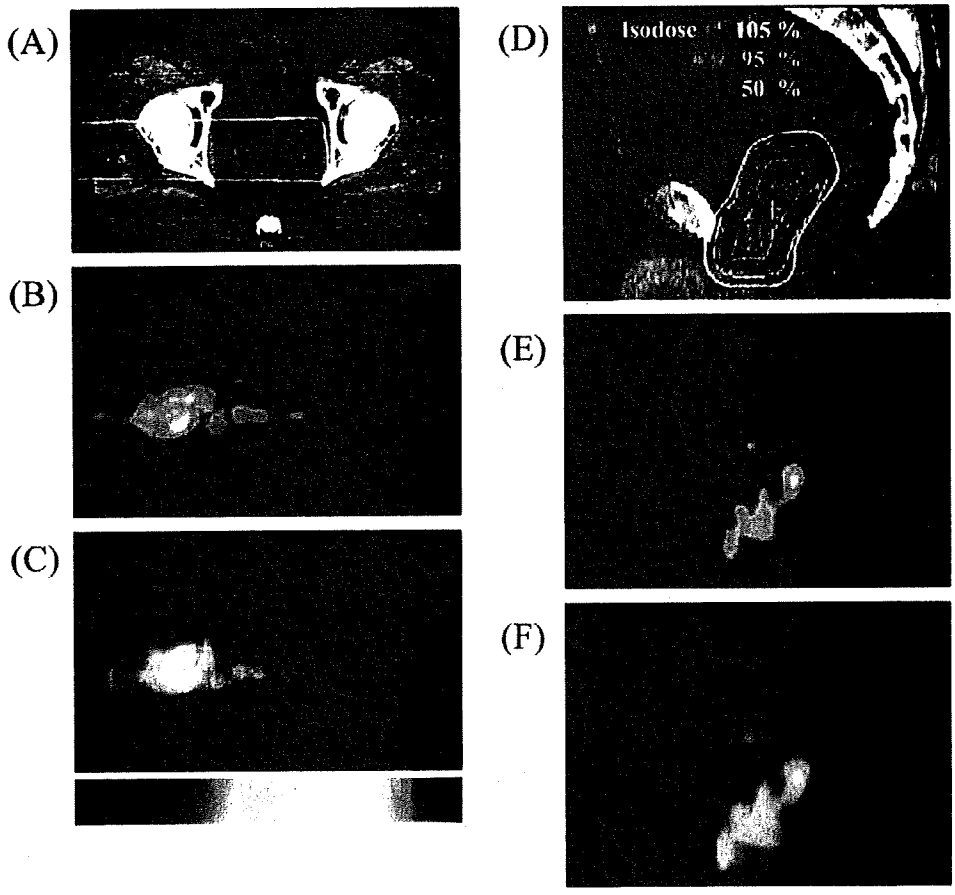

Fig. 1. Comparison of isodose curves and distribution of autoactivation in patients with prostate cancer (A) Axial image of calculated dose distribution in upper planning target volume (PTV) level. (B) Axial image of distribution of autoactivation in same PTV level. (C) Axial positron emission tomography (PET)/computed tomography (CT) fusion image. (D) Sagittal image of dose distribution (E) Sagittal image of distribution of autoactivation (F) Sagittal PET/CT fusion image.

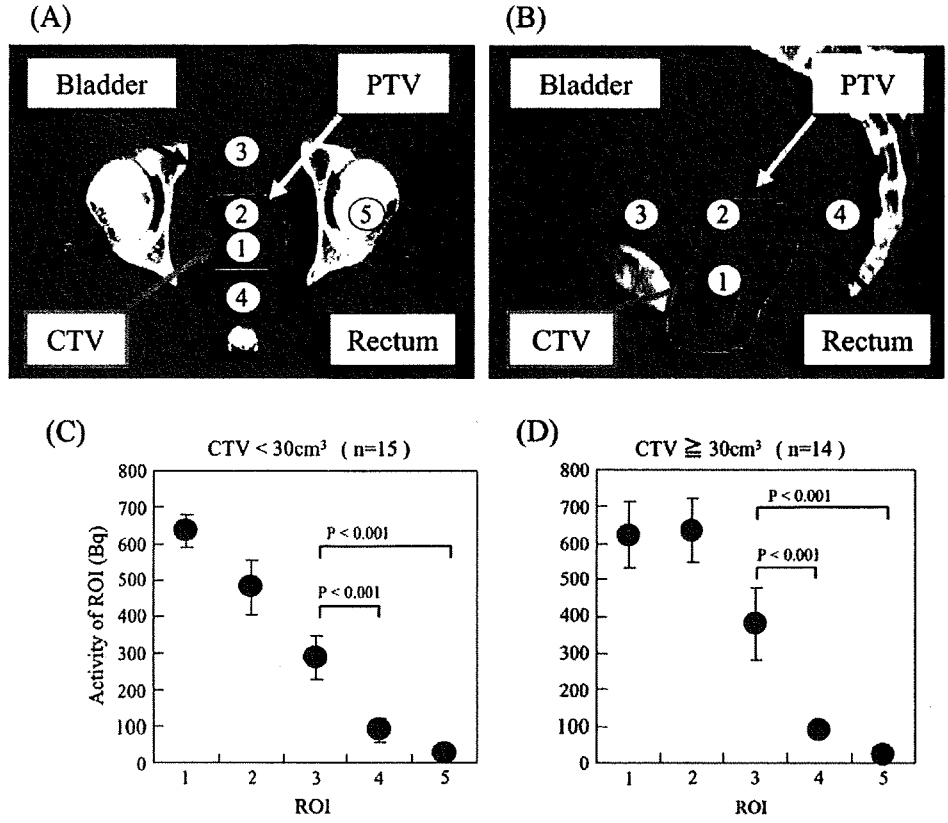

Fig. 2. Placement of regions of interest (ROIs) in 5 portions for calculation of activity measured by positron emission tomography: (1) planning target volume (PTV) center, (2) urinary bladder inside PTV, (3) urinary bladder outside PTV, (4) rectum, and (5) contralateral femoral bone head. (A) Axial and (B) sagittal images. (C and D) Results of calculation of 5 ROIs in two groups divided according to size of PTV (clinical target volume [CTV] <30 cm^3 [C] and CTV >30 cm^3 [D]).

95% isodose curve in terms of range, the detected autoactivation area seemed to spread outside the PTV, especially in the urinary bladder. On the sagittal images, the distribution of autoactivation also seemed to spread out in the urinary bladder.

Analyses of β^+ decayed nuclei distribution using clinical PET apparatus

To analyze the β^+ decayed nuclei distribution by use of the clinical PET apparatus, five areas (two inside the PTV and three outside the PTV, as described is "Methods and Materials" section) were drawn as ROIs (4 mm in diameter) based on the axial CT images (Figs. 2 A and 2B), and the radioactivity induced by autoactivation was counted in each ROI on PET axial images. The mean calculated activities in 29 patients were 629.3 Bq in the PTV center, 555.6 Bq in the urinary bladder inside the PTV, 332.5 Bq in the urinary bladder outside the PTV, 88.4 Bq in the rectum, and 23.7 Bq in the contralateral femoral head (Table 2). In the three regions outside the PTV (ROIs 3, 4, and 5 in Figs. 2A and 2B), the ROI on the urinary bladder (ROI 3) showed significantly higher activities than that on the rectum (ROI 4) or femoral bone head (ROI 5) regardless of CTV size ($p < 0.001$) (Figs. 2C and 2D). Quantitative analyses indicated that in our setting, the urine in the bladder could be a mode for diffusion of autoactivation after proton irradiation and may cause movement of the autoactivation signal.

Diffusion of autoactivation by proton beam therapy: Phantom study

To investigate the hypothesis regarding diffusion of autoactivation after proton irradiation, we planned a phantom experiment using water or an ice block. Figure 3 A shows the setting for a 6-cm SOBP in the context of 210-MeV proton beam irradiation or the same field size with 10 MV of X-ray irradiation. Activation was observed after proton irradiation but not after the same dose of X-ray irradiation (Figs. 3B and 3C). In the case of ice and water, activity decreased with time similarly, and the half-lives were 3.8 minutes for ice and 1.5 minutes for water (Fig. 3C).

Table 2. Radioactivity calculated using positron emission tomography apparatus after proton therapy (n = 29)

	Areas inside PTV*		Areas outside PTV*		
	PTV center	Urinary bladder inside PTV	Urinary bladder outside PTV	Rectum	Contralateral femoral head
Radioactivity (Bq)	629.3	555.6	332.5	88.4	23.7

Abbreviation: PTV = planning target volume.
* These regions of interest correspond with those shown in Figs. 2A and 2B.

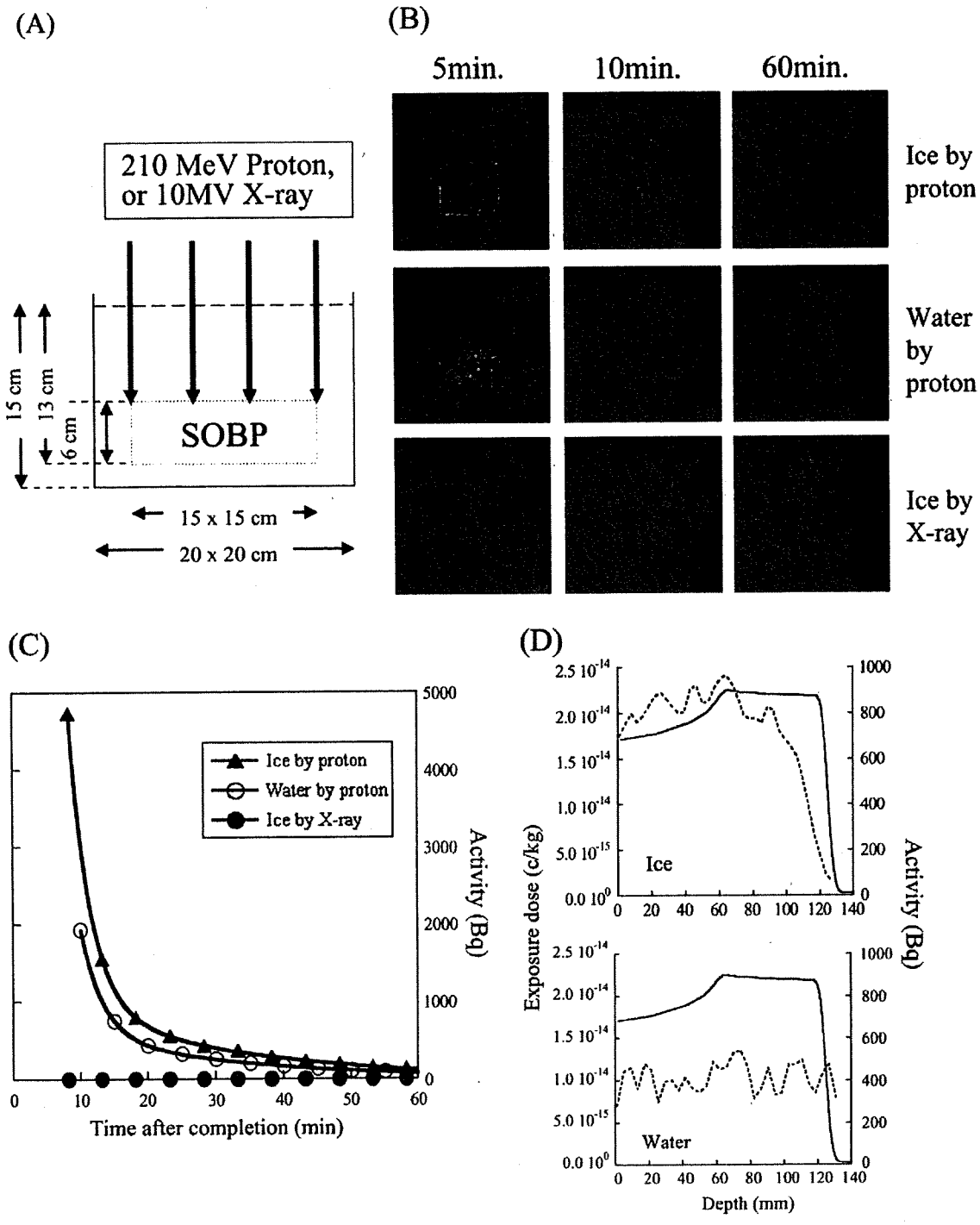

Fig. 3. Phantom study using water phantoms or ice blocks irradiated with 210-MeV proton beam or 10-MV X-ray. (A) Apparatus setup for irradiation. (B) Time course of autoactivation irradiated by protons in ice blocks, by protons in water, and by X-rays in water. (C) Time–activity curves in water and ice blocks after irradiation with 210-MeV proton or 10-MV X-ray beams. (D) Measured profile curves (dotted lines) indicating the direction parallel to the beam axis of β^+ decayed nuclei generated in the water phantoms or ice blocks compared with measured dose distribution (solid lines) by 210-MeV proton beam. SOBP = spread-out Bragg peak.

The extent of autoactivation in the ice block was observed only in the irradiated area (15 × 15 × 13 cm), whereas the autoactivation in the water was distributed throughout the phantom's volume (20 × 20 × 15 cm). The ratio between the volumes' observed autoactivation levels was 1:2.05. Regarding measured activity (10 minutes after completion), the ratio between the total counts of the ice block and the water was 1:0.55, despite both the water and the ice receiving the same dose and same field size of proton beam irradiation (Fig. 3C). The results of these reciprocal ratios indicated that β^+ decayed nuclei generated by proton irradiation within the irradiated volume do spread beyond the target area. In this

phantom experiment autoactivation images and counts diffused through the water but not the ice block, which may explain the results from the urinary bladders of patients receiving proton beam therapy. Figure 3D shows measured β^+ decayed nuclei and proton dose distributions in the ice block or water phantoms. The distribution of β^+ decayed nuclei in the ice block coincided with the dose distribution, whereas that in the water did not. This result also supports the notion that diffusion of activation needs to be taken into account when it is applied to proton beam verification.

Confirmation of autoactivation of urine

To obtain direct evidence of autoactivation in the urine, urine activity was measured in 30 patients. Figure 4 shows urine autoactivation over time. The half-life for autoactivation was 4.5 minutes, which was slightly longer than the ^{15}O half-life (2.0 minutes). This is probably because urine contains not only water (^{15}O) but other materials with ^{13}N (half-life, 10.0 minutes) or ^{11}C (half-life, 20.4 minutes). The urine activity measured in a well counter was 679.4 Bq by 10 minutes after the completion of the proton beam therapy, which was corrected for time-dependent decreases. These data were well matched with the data acquired from PET at 10 minutes after completion of the treatment.

DISCUSSION

We showed that proton beam therapy induced urine autoactivation that was detectible with PET in patients with prostate cancer. Autoactivation was generated by nuclear reactions such as the reactions of $^{12}C(p, pn)^{11}C$ and of $^{16}O(p, pn)^{15}O$ or nuclear fragmentation reactions such as the reactions of $^{16}O(p, x)^{11}C$, of $^{16}O(p, x)^{13}N$, and of $^{16}O(p, x)^{15}O$ (9). In our experimental setting and by use of our time points, the major component detected as a β^+ decayed nucleus by PET was defined as ^{15}O, not ^{11}C. The half-life of the activated urine was slightly longer than that of ^{15}O, probably because urine contains small amounts of protein, glucose, and ammonia, but the time course of decay was similar (Figs. 3C and 4). This half-life of the urine was well matched to that of water by use of the phantom. We therefore present direct evidence of autoactivation after proton beam therapy.

Several reports have shown the detection of autoactivation by PET after proton beam therapy (5, 7–11), including evaluating β^+ decayed nuclei without changing patient position (on-line system) (8, 10). These systems can achieve a high position resolution, with a field of view covering the isocenter of the beam irradiation system in the proton treatment room. The on-line phantom experiments indicated that PET imaging is sufficiently accurate for the verification of proton range and field lateral position (10). Although the range seemed to be grossly matched with the calculated dose in our clinical off-line system for patients with prostate cancer, distribution was not. Autoactivation was commonly observed outside the PTV, and in this study we have shown that this distribution results from autoactivation in the urine. As the cause of unexpected distribution of the β^+ decayed nuclei in the urinary bladder, three possible reasons might be raised: (1) diffusion in the urine, (2) movement of the patient (urine in the bladder) during transportation from the treatment room to the PET room, and (3) urinary injection from the ureter orifice to the bladder. Therefore detection of autoactivation with an on-line system seems to be more accurate than that using off-line systems. In either case, autoactivation of physiologic factors such as urine might affect PET imaging of the autoactivation. Although we have used the pencil beam algorithm, previous investigators reported that a CT-based Monte Carlo calculation of the dose delivery and its related PET imaging corresponded well to the treatment-planning dose and the measured PET distribution, producing deviations of only 1% to 5% between analytic and Monte Carlo dose calculations (11). These findings may establish a proton beam verification method in the future.

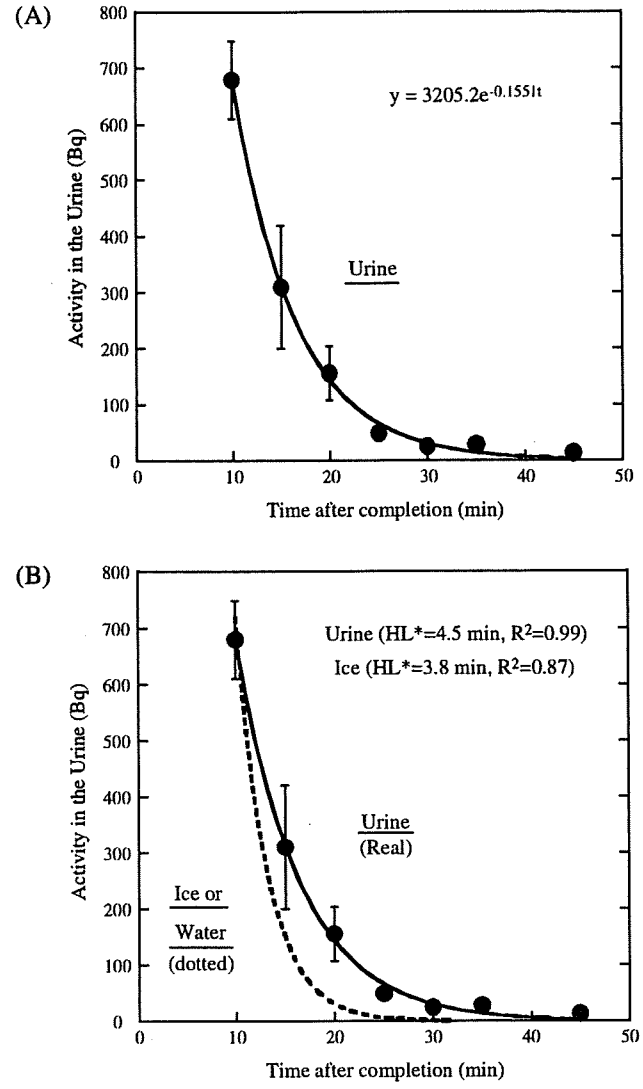

Fig. 4. (A) Time–activity curve of urine in patients with prostate cancer after proton beam therapy. (B) Activity of urine (solid line and circles) fitted to time–activity curve of ice or water (dotted line). The contribution ratios (R^2) were 0.87 for water and 0.99 for urine. HL = half-life .

We previously reported that the incidence of acute GU morbidity after proton beam therapy was similar to or slightly higher than that after intensity-modulated radiotherapy (6, 12–14). This result was unexpected because the majority of the urinary bladder was outside the PTV. Potential explanations are that the epithelial cells of the urethra in the prostate gland might undergo greater damage as a result of proton beam therapy or that the urethra might be compressed by the swelling of prostate glands induced by proton therapy. To examine another possible explanation, we tried to evaluate urinary autoactivation. As a result, the positron induced by the autoactivation in the urinary bladder was determined to be ^{15}O; however, the estimated absorbed dose was less than 1.0×10^{-6} cGy (15, 16). The dose of a single fraction seemed to be quite small to have influence on the urinary bladder or urethra. However, the influence of the sum of daily fractions remains undetermined, including whether activated urine may influence the epithelium of the urinary bladder, leading to acute GU morbidity. We are now planning a prospective study in which patients would urinate immediately after daily treatment to explore whether reduced acute GU morbidity exists. This test may require a large number of patients, but it could be an important step for establishing the use of proton beam therapy in the treatment of prostate cancer.

CONCLUSION

Positron emission tomography imaging of autoactivation allows for the verification of proton beam therapy. Urine is a major mode for the diffusion of autoactivation in patients with prostate cancer who undergo proton beam therapy. These results indicate that physiologic factors can influence PET images of autoactivation during verification of proton beam therapy.

REFERENCES

1. Raju MR. Proton radiobiology, radiosurgery and radiotherapy. *Int J Radiat Biol* 1995;67:237–259.
2. Yonemoto LT, Slater JD, Rossi CJ, *et al.* Combined proton and photon conformal radiation therapy for locally advanced carcinoma of the prostate: Preliminary results of a phase I/II study. *Int J Radiat Oncol Biol Phys* 1997;37:21–29.
3. Kagawa K, Murakami M, Hishikawa Y, *et al.* Preclinical biological assessment of proton and carbon ion beams at Hyogo Ion Beam Medical Center. *Int J Radiat Oncol Biol Phys* 2002; 54:928–938.
4. Hishikawa Y, Kagawa K, Murakami M, *et al.* The cancer treatment system at Hyogo Ion Beam Medical Center (HIBMC). *J Jpn Soc Ther Radiol Oncol* 2002;14:73–77.
5. Hishikawa Y, Kagawa K, Murakami M, *et al.* Usefulness of positron-emission tomographic images after proton therapy. *Int J Radiat Oncol Biol Phys* 2002;53:1388–1391.
6. Mayahara H, Murakami M, Kagawa K, *et al.* Acute morbidity of proton therapy for prostate cancer: The Hyogo Ion Beam Medical Center experience. *Int J Radiat Oncol Biol Phys* 2007;69:434–443.
7. Parodi K, Enghardt W, Haberer T. In-beam PET measurements of β^+ radioactivity induced by proton beams. *Phys Med Biol* 2002;47:21–36.
8. Litzenberg W, Roberts DA, Lee MY, *et al.* On-line monitoring of radiotherapy beams: Experimental results with proton beams. *Med Phys* 1999;26:992–1006.
9. Nishio T, Sato T, Kitamura H, *et al.* Distributions of β^+ decayed nuclei generated in the CH2 and H2O targets by the target nuclear fragment reaction using therapeutic MONO and SOBP proton beam. *Med Phys* 2005;32:1070–1082.
10. Nishio T, Ogino T, Nomura K, *et al.* Dose-volume delivery guided proton therapy using beam on-line PET system. *Med Phys* 2006;33:4190–4197.
11. Parodi K, Paganetti H, Shih HA, *et al.* Patient study of *in vivo* verification of beam delivery and range, using positron emission tomography and computed tomography imaging after proton therapy. *Int J Radiat Oncol Biol Phys* 2007;68:920–934.
12. Teh BS, Mai W, Uhl BM, *et al.* Intensity modulated radiation therapy (IMRT) for prostate cancer with the use of a rectal balloon for prostate immobilization: Acute toxicity and dose volume analysis. *Int J Radiat Oncol Biol Phys* 2001;49: 705–712.
13. Zelefsky MJ, Fuks Z, Hunt BA, *et al.* High-dose intensity modulated radiation therapy for prostate cancer: Early toxicity and biochemical outcome in 772 patients. *Int J Radiat Oncol Biol Phys* 2002;53:1111–1116.
14. Meerleer GD, Vakaet L, Meersschout S, *et al.* Intensity modulated radiotherapy as primary treatment for prostate cancer: Acute toxicity in 114 patients. *Int J Radiat Oncol Biol Phys* 2004;60:777–787.
15. Radiation dose to patients from radiopharmaceuticals. A report of a Task Group of Committee 2 of the International Commission on Radiological Protection. *Ann ICRP* 1987;18:1–377.
16. Radiation dose to patients from radiopharmaceuticals (addendum 2 to ICRP publication 53). *Ann ICRP* 1998;28:1–126.

別刷

癌と化学療法

VOL.36(2009)

癌と化学療法社

特 集 陽子線治療の現状と限界

兵庫県立粒子線医療センターの現状と将来展望

村上 昌雄[*1,2] 菱川 良夫[*1,2]

〔*Jpn J Cancer Chemother* 36(11): 1791-1794, *November*, 2009〕

Current Status and Future of Particle Radiotherapy at the Hyogo Ion Beam Medical Center: Masao Murakami[*1,2] and Yoshio Hishikawa[*1,2] (*[1]*Dept. of Radiology, Hyogo Ion Beam Medical Center (HIBMC)*, *[2]*Division of Ion Beam Therapy, Kobe University Graduate School of Medicine*)

Summary

The Hyogo Ion Beam Medical Center was established in May 2001, a leading project of the 'Hyogo Cancer Strategy'. Its major feature is that both proton and carbon ion beams can be generated. Particle beam radiation therapy had been performed in 2, 639 patients as of the end of March 2009. The diseases were prostate cancer, head and neck tumors, liver cancer, lung cancer, and bone soft tissue tumors, in decreasing order of frequency, and these 5 major diseases accounted for 87% of the cases. By beam-type therapy, 2, 122 and 517 patients (80 and 20%) were treated with proton and carbon ion beams, respectively. The outcomes surpassed those of surgical therapy realizing cancer therapy without resection. Current problems of particle beam radiation therapy include the unclear effect of differential use of proton and carbon ion beams and the necessity of laying in large-scale equipment, which prevents its dissemination. We are now aiming at the development and clinical application of a laser-driven proton radiotherapy device in cooperation with the Japan Atomic Energy Agency. **Key words**: Proton radiotherapy, Carbon-ion radiotherapy, Particle radiotherapy, **Corresponding author**: Masao Murakami, Department of Radiology, Hyogo Ion Beam Medical Center (HIBMC), 1-2-1 Kouto, Shingu-cho, Tatsuno, Hyogo 679-5165, Japan

要旨 兵庫県立粒子線医療センターは「ひょうご対がん戦略」のリーディングプロジェクトとして計画され，9年を経て2001年5月に開院した。最も大きな特徴は世界で初めて陽子線と炭素イオン線の両者を使用できることである。2009年3月末までに2,639名に粒子線治療を行った。対象疾患は前立腺がん，頭頸部腫瘍，肝がん，肺がん，骨軟部腫瘍の順に多く，これらの5大疾患だけで87%を占める。線種の内訳は陽子線2,122名(80%)，炭素イオン線517名(20%)であった。治療成績は手術療法を凌駕しており，切らずに直すがん治療が実現しつつある。現時点の粒子線治療の問題点は陽子線と炭素イオン線の使い分けがはっきりしないこと，装置が大がかりで普及の障害になっていることである。われわれは日本原子力開発機構と共同でレーザー駆動陽子線治療装置の開発，臨床適用をめざしている。

はじめに

粒子線治療は，日本および諸外国の36施設において，延べ57,000名以上の患者に対して行われている。そのうち9施設はすでに治療を終了し，現在稼働中の施設は27施設となっている。日本においては7施設が稼働しているが，今後海外で15施設，国内では少なくとも4施設の建設が予定されている。

粒子線はブラッグピーク（Bragg peak）と呼ばれる物理学的な特徴があり，加速エネルギーに応じて体内のある一定の深さでピークを形成する。ビーム軸方向でブラッグピークを超えた領域への被爆は皆無であり，皮膚面からブラッグピークが立ち上がるまでのエントランス部分においても，腫瘍線量より低い線量に抑えることができる。これは従来のX線，ガンマ線，電子線にはない特徴である。この性質を利用すれば，周囲の正常組織のダメージを最小限度に抑えながら病巣に限局性に高線量を集中できる。粒子線治療は従来の放射線治療に比べる

*1 兵庫県立粒子線医療センター・放射線科
*2 神戸大学大学院医学系研究科・放射線医学分野粒子線医学部門

連絡先: 〒679-5165 たつの市新宮町光都1-2-1 兵庫県立粒子線医療センター・放射線科
村上 昌雄

と治療効果が高く副作用が少ない治療であるため，手術に取って代わる局所療法として期待されている[1]。

X線は単位長さ当たりに与える平均エネルギーが低い放射線（低LET放射線）といわれている。陽子線治療や炭素イオン線はX線より単位長さ当たりに与える平均エネルギーが高い。そのため粒子線はX線に比べ放射線損傷が回復しにくく，組織内酸素濃度や細胞周期の影響を受けにくいという特徴がある。すなわちX線を1とした場合に対する陽子線，炭素イオン線の相対的生物学的効果比（RBE: relative biological effectiveness）はそれぞれ1.1，3.0と見積もられており，いわゆる放射線抵抗性腫瘍にも効果が期待できる。

Ⅰ．兵庫県立粒子線医療センターの概要

兵庫県立粒子線医療センターは「ひょうご対がん戦略」のリーディングプロジェクトとして計画され，9年を経て2001年5月に開院した。2002年10月末には陽子線に関する治療装置の製造承認が下り，2003年4月から陽子線の一般診療が開始されることとなった。この後，炭素線については2005年1月に治療装置の製造承認が下り，3月から一般診療を開始している。さらに，陽子線は2004年7月，炭素線は2005年5月にそれぞれ高度先進医療の承認を得ることができ，入院・検査料などについて保険適用となった。治療装置の製造承認が得られてから高度先進医療の承認が得られるまでの1年余りの期間は保険適用がなかったが，患者負担を減らすべく県費で保険負担相当額をまかなった。

特徴は，①全国自治体初の粒子線治療施設，②世界で初めて陽子線と炭素イオン線の両者を使用できることである。常勤スタッフは45名で内訳は，医師7名，放射線技師12名，医学物理士2名，加速器物理士1名，薬剤師1名，看護師18名，事務4名である。その他，非常勤の医師4名，技師2名，看護師1名，装置のQA，線量測定，装置運転を主務とする運転委託業者職員13名，医事および治療終了後の経過観察を担当する委託事務職員7名を擁している。

運営方針（病院の理念）は①がんの治癒率を改善するとともに，がん患者の社会復帰を目指す，②比較的早期の原発がんを第一の適応とする，③病院らしくない病院にする，④世界に開かれた病院にする，⑤世界に向けて新しい粒子線治療の情報発信地にする，の5項目である。

Ⅱ．治療基準

治療の適応疾患，治療法などは治療基準に従って判断している。各領域の専門家を中心とした治療基準策定委員会を定期的に開催し，治療基準の見直し，追加修正を行っている。基本的には局所に限局した固形がんが適応となる。胃や大腸がんなど蠕動があり正確に照準できない消化管腫瘍や喉頭がんのように従来の治療法が確立されている腫瘍は適応とならない。頭蓋底腫瘍，頭頸部腫瘍，肺がん，肝がん，前立腺がん，骨軟部腫瘍が適応疾患の主なものである。

Ⅲ．治療計画と治療検証

治療の準備には固定具作製，CT，MRI撮影，治療計画装置を用いた線量計画，ボーラスコリメータ作製，リハーサル，線量測定のために1週間を要する。開院当初は医師が治療計画を行っていたが，現在は診療放射線技師，医学物理士，医師の3者が共同して行い，毎日治療計画カンファレンスで最終決定している。安全・確実・恒常性があり，後日の評価に耐え得る治療計画を作成するためには必要不可欠なチームと考えている。粒子線治療は通常の放射線治療とは異なり，ビーム停止の位置・形状を任意に形成することができる。線量計算値と実測値が一致しているかどうか，患者ごとにすべての門の線量分布を事前に水ファントムを用い実測検証を行い，かつ初回照射直後には自己放射化現象を利用した線量分布の確認を行っている。粒子線治療を行うと照射部位に核の分裂が生じる。たとえば陽子が照射されると体を構成する酸素原子，炭素原子はそれぞれ^{16}O (p, pn)^{15}O，^{12}C (p, pn)^{11}Cの反応でポジトロン核種を生じる。炭素イオン線照射の場合は照射する炭素イオン自身がprojectile fragmentationを来し^{11}Cを生じる。^{15}Oは半減期が2分，^{11}Cは半減期が20分であるため，当センターでは初回治療直後にPET撮影を行い，治療計画画像と対比させ検証作業を行っている[2]。

Ⅳ．経過観察

一般にがん治療後の5〜10年にわたる経過観察は重要である。粒子線治療のように全国から患者が来院する施設では，地域医療を対象とした従来型病院の経過観察システムでは対応できない。そこで当センターでは経過観察担当医を中心として看護師，事務からなるチーム医療を行っている。治療を終了した患者には「患者カルテ＝自分のカルテ」を渡している。そのなかには病歴，粒子線治療の実施記録，粒子線治療の照射部位を記載した線量分布図，血液・尿検査データ，腫瘍を示す臨床画像（CTやMRI），問診表，連絡表などが入っており，患者と当センターの郵送による経過観察システムの中心をなす。普段は患者の手元において自身の健康管理に活用してもらう。当センターで行った治療の全般がそこに記載されているだけでなく，治療後の経過も画像や血液検査データ

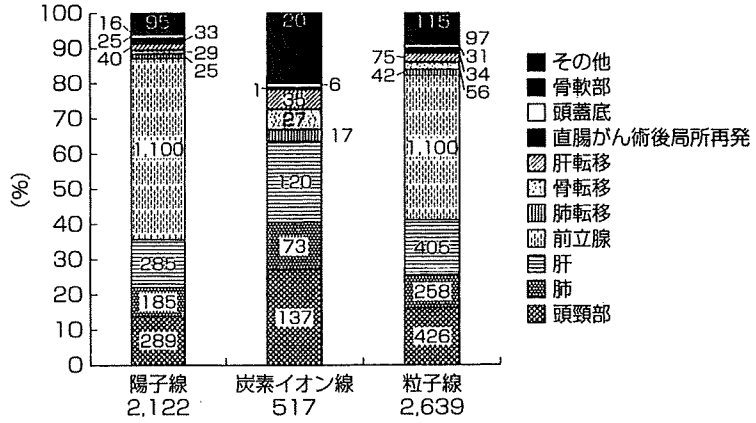

図1　線種別疾患内訳（2001年～2009年3月）

などで把握できるようになっている。当センターに届いた「患者カルテ」や臨床画像などは経過観察室で取りまとめられ，電子保管される。患者カルテに新しいデータを追記した後，患者宅にすべてを返却するという仕組みである。顔をみながらの診察ではないが，それを補う目的で問診表や連絡簿あるいは皮膚写真などを活用している。しかしイベント発生時には外来受診してもらい直接診察を行っている。また電話での相談にも応じており，経過観察担当看護師，医師が対応している。このシステムはよく機能しており，経過観察脱落例はほとんどない。

V. 治療実績

2009年7月現在，2,800名を超える患者を治療している。2009年3月時点（総計2,639名）の統計では，線種の内訳は陽子線2,122名（80%），炭素イオン線517名（20%）であった（図1）。炭素イオン線が少ないのは一般診療開始時期が陽子線より約2年遅れたことと，ガントリーが使えないこと，炭素線の最大エネルギーが320 MeVではレンジが15 cmのため，前立腺がんなどの深在性腫瘍を照射できないという制限があるためである。ただし最近は炭素イオン線の適用例が増えつつあり，最近の1年では36%と増加していた。これは，頭頸部腫瘍や肺，肝がんでは，同一症例に陽子線と炭素イオン線の両者の治療計画を行い，線種選択の一助としているが，炭素イオン線は核破砕現象を認めるものの側方散乱が少ないため，多くの場合陽子線よりビームの切れはよく，線量集中性はよくなることが多いためである。

疾患の内訳は前立腺がん1,100名（41.7%）が最も多く，以下，頭頸部426名（16.1%），肝405名（15.3%），肺258名（9.8%），骨軟部腫瘍97名（3.7%）の順で，これらの5大疾患だけで87%を占める。もっとも対象疾患は増えつつある。たとえば孤立性の遠隔転移も予後との兼ね合いをみて治療を行っている。また最近では，神戸大学肝胆膵外科と協力し，消化管障害を防止するためスペーサー留置を行い腹部臓器がんに対する適応拡大を行っている。

骨肉腫などの骨軟部腫瘍にも根治的治療が可能であることや，頭頸部腫瘍でも悪性黒色腫，腺様嚢胞がん，腺がんなど放射線抵抗性と考えられる腫瘍が扁平上皮がんより多くを占めることが，X線による放射線治療を行っている施設とは異なる特徴である。肺がんでは1期を主な対象として治療してきたが，パンコースト肺がんなどのT3，T4肺がんも適応になる。肝がんに関しては13 cm未満の単発腫瘍を適応としており，数cm大の比較的大きな肝がんが中心となるが局所制御率90%という好成績が得られている。治療中の急性反応は軽微で，頭頸部腫瘍患者でもほぼ全例において経口摂取が可能であり，外来通院治療が全患者の約4割に達することからみても体に優しいがん治療が実現できているといえる。

VI. 当センターの主要課題と将来展望

主要課題は，①陽子線・炭素線治療の促進，②医療安全の確保，③治療装置の安定稼働，④粒子線治療普及の推進である。

①当センターは陽子線と炭素線両者を使用できるが，その使い分けをめぐる問題は未解決である。処方線量・分割に関しては，従来の粒子線治療施設で安全・有効と判断されたものを採用してきたので，陽子線と炭素イオン線のプロトコールに差があり，厳密な比較はできない。しかしそれを承知で各種疾患の成績を検討したところ，効果，予後，晩期有害事象に明らかな差を認めていない[3,4]。今後は各疾患において同一線量分割を用いた比較試験を実施してゆく予定である。

②治療患者数の増加に伴い，50床のベッドは満床となり外来照射が増えている。宿泊施設の利用や近隣医療機関との連携で対応しているが，他院の医師・看護を含

めた医療連携が重要課題となっている。今年から膵がんや進行肝がんに対して抗がん剤併用粒子線治療を試みている。今後，各種局所進行がんに対して適応拡大が進んでゆけば，なおさら医療安全の観点からみた連携が重要となってくる。

③粒子線治療施設の泣きどころは治療機器の致命的なトラブルがあった場合に代替機が用意されていないことである。幸い今までそのような事態に直面していないが，南東北病院陽子線治療センターや来年度開院予定のメディポリス粒子線治療センターとは粒子線施設間連携を進めている。

④粒子線治療は大規模な設備が必要で，以前は物理研究所における医学利用に限られていたが，1990年以後，病院設置型装置が導入されるようになり，徐々に医療の現場に参入しつつある。しかし現時点では患者医療費負担は高度先進医療下でも約300万円と高額であり，保険診療への発展が望まれる。そのためには建設費，維持費を低減化させた普及機器の開発，人材育成が必要である。シンクロトロンやサイクロトロンを用いないレーザー駆動型加速器は1979年Tajimaら[5]により提唱され，医学利用のための加速器開発が進められつつありテーブルトップサイズの加速器も夢ではない。さらにスポットスキャンニングに代表される粒子線照射技術とimage guided treatment planning手法が発展融合すれば，まさに個々の腫瘍の感受性や難治度に見合った個別化粒子線治療を行える日も近い[6]。

文　献

1) 阿部光幸，菱川良夫，村上昌雄：陽子線と炭素線治療—癌患者の速やかな社会復帰を目指す．実験医学　22：2111-2116，2004.
2) Hishikawa Y, Kagawa K, Murakami M, *et al*: Usefulness of positron-emission tomographic images after proton therapy. *Int J Radiat Oncol Biol Phys*　53: 1388-1391, 2002.
3) Miyawaki D, Murakami M, Demizu Y, *et al*: Brain injury after proton therapy or carbon ion therapy for head and neck cancers and skull base tumors. *Int J Radiat Oncol Biol Phys*　75: 378-384, 2009.
4) Demizu Y, Murakami M, Miyawaki D, *et al*: Analysis of vision loss caused by radiation-induced optic neuropathy after particle therapy for head-and-neck and skull-base tumors adjacent to optic nerves. *Int J Radiat Oncol Biol Phys*　(epub ahead of print), 2009.
5) Tajima T and Dawson JM: Laser electron accelerator. *Phys Rev Lett*　43: 267-270, 1979.
6) Murakami M, Hishikawa Y, Miyajima S, *et al*: Radiotherapy using a laser proton accelerator. (eds by Bulanov SV, Daido H), AIP conference proceedings, 1024, Melville, New York, 2008, pp275-300.

ELSEVIER

Int. J. Radiation Oncology Biol. Phys., Vol. 75, No. 2, pp. 564–570, 2009

0360-3016/09/$–see front matter

doi:10.1016/j.ijrobp.2009.03.074

5TH JUCTS AND THE 5TH S. TAKAHASHI MEMORIAL INTERNATIONAL JOINT SYMPOSIUM

RESIDUAL MOTION AND DUTY TIME IN RESPIRATORY GATING RADIOTHERAPY USING INDIVIDUALIZED OR POPULATION-BASED WINDOWS

HIROSHI FUJI, M.D., PH.D.,* YOSHIHIRO ASADA, R.T.T.,* MASUMI NUMANO, R.T.T.,* HARUO YAMASHITA, PH.D.,* TETSUO NISHIMURA, M.D., PH.D.,† TAKAYUKI HASHIMOTO, M.D.,‡ HIDEYUKI HARADA, M.D.,† HIROFUMI ASAKURA, M.D.,† AND SHIGEYUKI MURAYAMA, M.D., PH.D.*

*Proton Therapy Division and †Radiation Oncology Division, Shizuoka Cancer Center, Nagaizumi, Shizuoka, Japan; and ‡Department of Radiation Oncology, University of Tsukuba, Tsukuba, Ibaraki, Japan

Purpose: The efficiency and precision of respiratory gated radiation therapy for tumors is affected by variations in respiration-induced tumor motion. We evaluated the use of individualized and population-based parameters for such treatment.

Methods and Materials: External respiratory signal records and images of respiration-induced tumor motion were obtained from 42 patients undergoing respiratory gated radiation therapy for liver tumors. Gating window widths were calculated for each patient, with 2, 4, and 10 mm of residual motion, and the mean was defined as the population-based window width. Residual motions based on population-based and predefined window widths were compared. Duty times based on whole treatment sessions, at various window levels, were calculated. The window level giving the longest duty time was defined as the individualized most efficient level (MEL). MELs were also calculated based on the first 10 breathing cycles. The duty times for population-based MELs (defined as mean MELs) and individualized MELs were compared.

Results: Tracks of respiration-induced tumor motion ranged from 3 to 50 mm. Half of the patients had larger actual residual motions than the assigned residual motions. Duty times were greater when based on individualized, rather than population-based, window widths. The MELs established during whole treatment sessions for 2 mm and 4 mm of residual motion gave significantly increased duty times, whereas those calculated using the first 10 breathing cycles showed only marginal increases.

Conclusions: Using individualized window widths and levels provided more precise and efficient respiratory gated radiation therapy. However, methods for predicting individualized window levels before treatment remain to be explored.

Adaptation, Liver tumor, Organ motion, Respiratory gating, Radiotherapy.

INTRODUCTION

Local control of liver tumors has been reported using extracranial stereotactic radiotherapy or particle-beam therapy (1–12). Some of these studies addressed the feasibility of using radiotherapy for liver tumors and whether it could be improved by reducing the irradiated liver volume using conformal irradiation (1, 2, 5). However, tumor motion due to respiration is known to affect the actual radiation dose delivered and to distort the reduction in planning target volumes for small-dose baths (13–15). The track of liver tumors due to respiration is known to range from 10 to 30 mm, which is greater than the 5- to 20-mm range for lung tumors (15–17). On account of this motion, liver tumors may require more advanced motion management strategies when simulating, planning, and treating these tumors, compared with tumors in other anatomic site (16, 18–24)

Respiratory gated radiotherapy is one of several effective techniques for the management of respiratory motion (1, 2, 18, 22, 25). The theoretic basis is this: When a patient is treated with respiratory gating, there is a tradeoff between residual motion of the tumor and the efficiency of treatment delivery. The allowed range of motion is the gating window, which can be range of respiratory phase or amplitude of the tumor or an external surrogate. This article will discuss only amplitude-based gating (16, 20, 21, 26, 27).

Most reports that have investigated the feasibility of this therapy have adopted a window width between 1% and

Reprint requests to: Hiroshi Fuji, M.D., Ph.D., Proton Therapy Division, Shizuoka Cancer Center, 1007 Shimonagakubo, Nagaizumi, Shizuoka, 411-8777, Japan. Tel: (+81) 55-989-5222; Fax: (+81) 55-989-5634; E-mail: h.fuji@scchr.jp

Conflict of interest: none.

Received Aug 14, 2008, and in revised form March 17, 2009. Accepted for publication March 19, 2009.

40% of the amplitude of the respiratory signal (20, 28, 29). For a respiration-induced tumor track of 10–30 mm, the residual motion corresponds to 0–12 mm residual motion. The range of residual motion exceeds values to be adopted in gated treatment according to the recommendation of the American Association of Physicists in Medicine (16). Using a standard gating window setting, therefore, may lead to unacceptable levels.

Another important issue for optimizing respiratory gated radiation therapy is the timing of the gating window. To reduce residual motion while a respiratory signal is in the window, the end of the exhalation phase is generally used to determine the timing of gating, because deviations in the tumor position are slow during this phase of the breathing cycle (20, 28, 29). Furthermore, the amplitude of respiration at the end of exhalation is known to be more reproducible than those during inhalation or any other phase of respiration. However, an issue encountered when gating with a small window at end exhalation is baseline drift, which could cause a fixed amplitude window for the respiration surrogate that no longer corresponds to the patient's true end exhalation phase. This not only leads to the possibility of a geometric miss but also results in a very low duty cycle because the patient quickly passes through the gating window on the way to true end exhalation.

Applying standard respiratory window widths and window levels does not achieve the most precise and efficient delivery of radiotherapy in many patients. To accommodate the variety of tumor tracks due to respiration and different breathing patterns, adaptive respiratory gated radiotherapy needs to be developed. The current study investigated the use of individualized parameters for respiratory gating to improve the precision and efficacy of radiotherapy.

METHODS AND MATERIALS

Patients

In this study we computed the most efficient level (MEL) based on both the patient's first 10 breathing cycles and also based on the entire treatment. We then retrospectively simulated respiratory gating for each of these gating windows and also for a population-based window (Fig. 1). The experimental plan for comparing the individual and population-based gating settings for treatment is shown in Fig. 1. These retrospective data analyses and simulations were approved by the Review Board at the Shizuoka Cancer Center, Japan. Between June 2005 and July 2006, 80 patients underwent proton-beam therapy for liver tumors using the respiratory gating technique, according to an institutional review board protocol for clinical practice and with the informed consent of all patients. Of the 80 patients, 42 individuals for whom surrogate positioning markers had been used were selected for inclusion in the study. In 41 patients, 2-mm fiducial markers had been implanted near the tumors. Surgical clips near the tumors were used as surrogate positioning markers in 1 patient. The characteristics of the patients are shown in Table 1. Their performance status was 0–1, their median age was 60 years, and 40% were older than 70 years. Two patients had clinically apparent pulmonary emphysema.

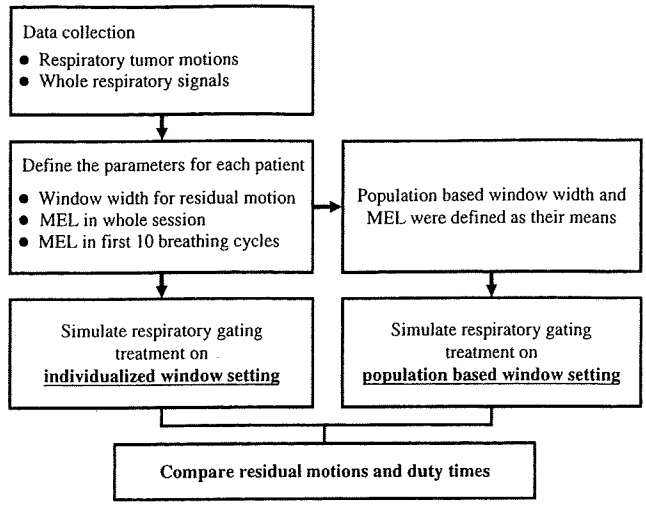

Fig. 1. Flow chart for comparing the precision and efficiency of using individualized and population-based respiratory gating window settings. MEL = most efficient level.

Respiratory data collection

External respiratory signals were obtained by monitoring abdominal wall movement. The height of the abdominal wall was measured using an infrared laser distance meter targeting the upper abdomen, and was recorded throughout every treatment session. For this analysis, respiratory records from the fifth treatment sessions were used, to avoid the interruptions in treatment that occurred during early sessions when respiration training was carried out. The first 10 breathing cycles were used for normalization, and the mean amplitudes at the end of exhalation and inhalation in the 10 breathing cycles were determined as 0% and 100% amplitude of respiration, respectively.

Tracking tumor movement and residual motion

Fiducial markers or other radiopaque materials in the liver were used as surrogates for tumor position. Two orthogonal fluoroscopes recorded vertical and horizontal images of the markers. It should be noted this group of patients had been trained to breath slowly, and 3.5 frames/s gave us approximately 20 samples per breathing cycle. After checking the stability of the depth and track of respiration for at least three breathing cycles, images of the positioning markers

Table 1. Patient characteristics (n = 42)

Median age (range)	72 (50–90)
Sex	
Male	31
Female	11
Disease	
Hepatocellular carcinoma	39
Cholangiocellular carcinoma	2
Liver metastasis	1
Liver cirrhosis (Child-Pugh class)	
A	36
B	6
cTNM	
T1N0M0	34
T2N0M0	6
T3N0M0	1
T0N0M1	1

were recorded at 3.5 frames/s over one breathing cycle. At the same time, synchronized external respiratory signals were recorded. The respiratory signal amplitudes at the end of exhalation and inhalation were defined as 0% and 100%, respectively. Linear regression formulas for tumor position and respiratory signal (amplitude-based) were established from the fluoroscopic images and normalized respiratory signals. Window widths of respiratory signal (amplitude-based) corresponding to residual motions of 2, 4, and 10 mm were calculated using the measured data for each patient. The mean tumor track was calculated for all patients and was used to calculate the population-based window width for residual motion as a percentage of the residual motion. The ranges of residual motion in all patients when the population-based and general window widths were applied were calculated. The residual motions with individualized window widths and a population-based window width were compared.

Establishing the most efficient level (MEL) in external respiratory signals

In the current study, the window level was defined as the lower end of the respiratory gating window. A previously published study of respiratory gated radiotherapy suggested that window levels were generally set at the end of exhalation, as 0% amplitude, for long duty times (28–30). However, the MEL varies for each respiratory signal pattern and for each window width. Therefore, the duty times for window widths were calculated from −40% to +40% of the window levels in each patient, and the window level with the longest duty time was defined as the MEL for each patient. This MEL was based on a respiratory signal from a whole treatment session (IW-MEL). In this work we calculated MELs in three ways: for the entire respiratory history over a given treatment (IW-MEL), for the early part of the treatment (IF-MEL), and population based (P-MEL). The IF-MEL was calculated using the first 10 breathing cycles in a given treatment. The P-MEL was the mean of each patient's MEL for the whole treatment session. To assess the predictive accuracy of MELs calculated from the early part of the respiratory cycle, respiratory signals from the first 10 breathing cycles were used (IF-MEL). The P-MEL used for each residual motion was the mean of each patient's MEL for the whole treatment session.

Comparison of duty time and residual motion

The duty times for individualized window width and population-based window width were compared for a window level of 0% to avoid the influence of window level optimization. The duty times were compared for individualized MELs (IW-MELs and IF-MELs) and P-MELs and for a general window level of 0% amplitude to find an efficient window level setting. Statistical analyses were carried out using SPSS statistic software version 11 J (SPSS, Chicago, IL).

RESULTS

Respiratory tumor motion and residual motion

The tracks of respiration-induced tumor motion in 42 patients ranged from 3.0 to 50.2 mm, and the mean track length was 15.3 mm (Fig. 2). The mean window widths calculated for 2, 4, and 10 mm residual motion ($WW_{(2\ mm)}$, $WW_{(4\ mm)}$, and $WW_{(10\ mm)}$, respectively) from the mean respiratory tumor tracks were 16%, 31%, and 78%, respectively. The variations in the actual residual motion for the mean $WW_{(4\ mm)}$ are shown in Fig. 3. Half of the patients had larger actual residual motions than the assigned residual motions. Five patients in the cohort of 42 showed residual motion that was more than 150% larger than expected. Two patients showed residual motion that was more than twice that expected. The proportion of patients showing far greater residual motion at $WW_{(2\ mm)}$ and $WW_{(10\ mm)}$ was similar to that at $WW_{(4\ mm)}$.

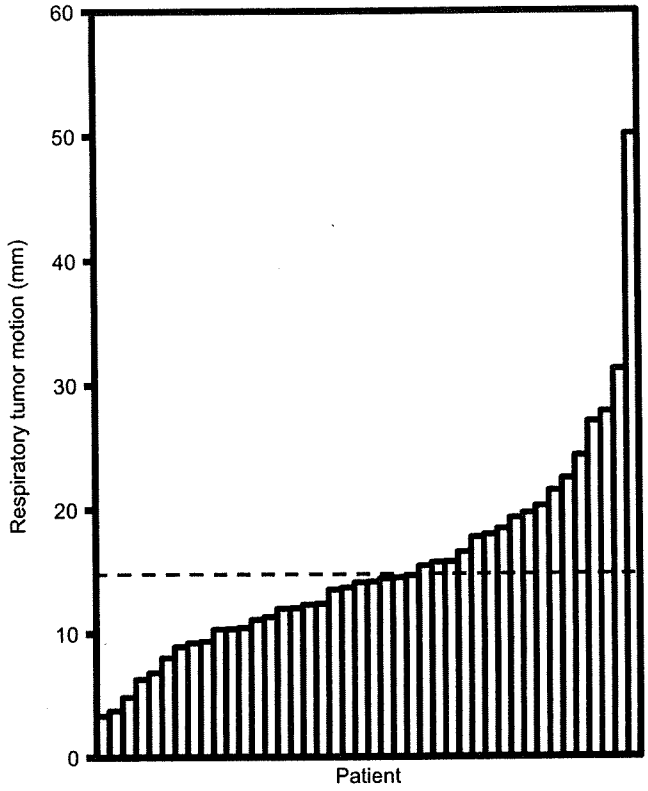

Fig. 2. Respiration-induced tumor motion for each patient. The dotted line represents the mean tumor motion.

MEL for respiratory gating window

The window levels were specified to give the most efficient treatment at $WW_{(2\ mm)}$, $WW_{(4\ mm)}$, and $WW_{(10\ mm)}$. The mean MELs for both whole treatment sessions and the first 10 breathing cycles are shown in Table 2. In both cases, the MELs calculated were less than 0%, with the values decreasing as the window width increased. The MELs at assigned window widths were affected by both the baseline stability, namely the end of exhalation, and the shape of the respiratory signals.

In patients who showed low baseline variations, the histogram demonstrated that tumor was predominantly located around 0%, end-of-exhalation phase (Fig. 4, case 1). Therefore, a longer duty time could be obtained in these cases even with small window width. The respiratory signal was negative for only a small proportion of the treatment time. By contrast, when the respiratory signal showed a greater variation in baseline, a considerable proportion of the treatment time fell below 0% at larger residual motion (Fig. 4, Patient

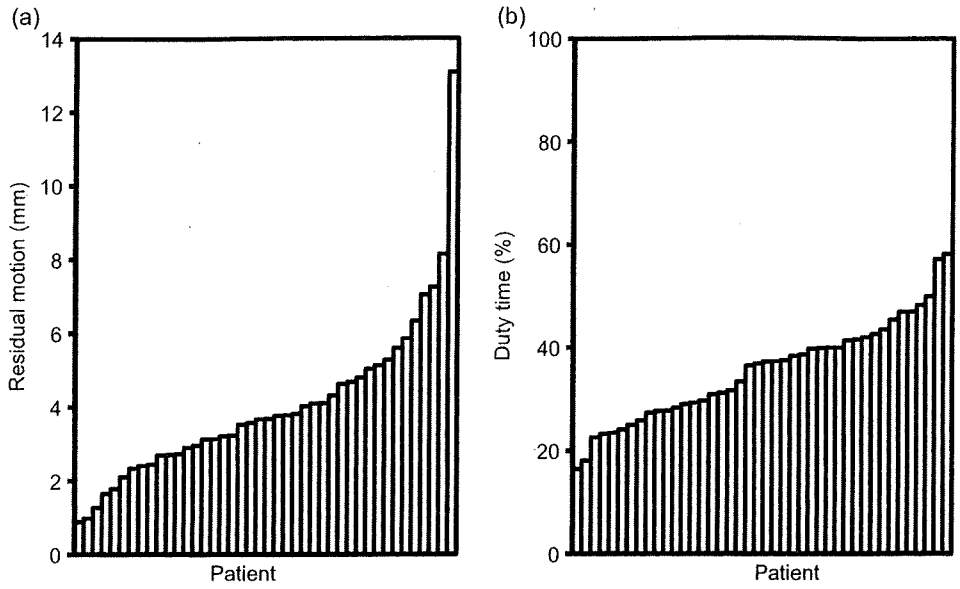

Fig. 3. Simulations of respiratory gated radiation therapy. (a) Residual motion using a population-based common window width for 4 mm of residual motion. (b) Duty time using an individualized window width for 4 mm of residual motion.

2). At this setting, the window shifted both upward and downward as the window width increased.

Duty time evaluation

Mean duty time increased as larger window width was applied in both individualized and population-based window width settings (Table 3). For this cohort with average tumor motion of 13.5 mm, the mean duty time was less than 70% even for 10 mm of residual motion. The mean duty times calculated using individualized window widths and residual motions of 2, 4, and 10 mm were significantly longer than the mean duty times calculated on a population basis.

The duty times for different types of window level are shown in Tables 4 and 5. Individualized MELs (IW-MELs, IF-MELs) and P-MELs provided significantly longer duty times than were observed for a window level of 0%, with the exception for $WW_{(2\ mm)}$. The duty times for individualized MELs based on whole sessions using $WW_{(2\ mm)}$ and $WW_{(4\ mm)}$ were significantly greater than those for the P-MELs. By contrast, the individualized MELs based on the first 10 breathing cycles did not result in significantly longer duty times than the population-based window level at $WW_{(4\ mm)}$ and $WW_{(10\ mm)}$. To evaluate the predictive capability of IF-MEL for IW-MEL, the relationships between IF-MEL and IW-MEL were calculated. The relationship of MELs for $WW_{(2\ mm)}$, $WW_{(4\ mm)}$, and $WW_{(10\ mm)}$ were significant ($p < 0.001$), and Pearson's correlation coefficients were 0.662, 0.502, and 0.490, respectively.

Table 2. Maximum efficient levels for residual motion

Residual motion (mm)	Whole treatment session (%)	First 10 breathing cycles (%)
2	−0.6 (−9.0 to 11.0)	−2.0 (−7.0 to 7.0)
4	−3.0 (−12.0 to 9.0)	−3.3 (−8.0 to 5.0)
10	−5.9 (−33.0 to 8.0)	−4.4 (−16.0 to 8.0)

DISCUSSION

Respiratory gated radiotherapy provides great advantages for patients with liver tumors; however, the introduction of common, and therefore arbitrary, gating parameters means that in some cases there is unacceptable residual motion. Adaptive respiratory gated radiotherapy, using individualized respiratory gating parameters and predefined residual motion, is expected to offer the most efficient and precise irradiation of liver tumors. To explore the effectiveness of the adaptive technique, we simulated respiratory gated radiation therapy with the data of tumor tracks and records of respiratory signal.

The current study of the effectiveness of adapting the technique to variations in respiration addressed three aspects of characterizing respiration that might have therapeutic advantages. First, the precise evaluation of respiratory motion was investigated. Tumor motion was evaluated using radiopaque positioning markers and fluoroscopy. Simultaneous orthogonal views were recorded after checking the stability of tumor motion. Respiration-induced tumor motion was observed to be rapid, and its speed also fluctuated. Therefore, if tumor motion is measured by a method that involves substantial interruptions in obtaining sequential images, there is a possibility that it will fail to define peak motion, which should be taken into account. The fast acquisition of images by fluoroscopy is a more appropriate method from this point of view. Furthermore, the use of orthogonal images with excellent spatial resolution and surrogate positioning markers has been shown to provide more accurate data on tumor position than either electroportal imaging or computed tomography (14, 30–32).

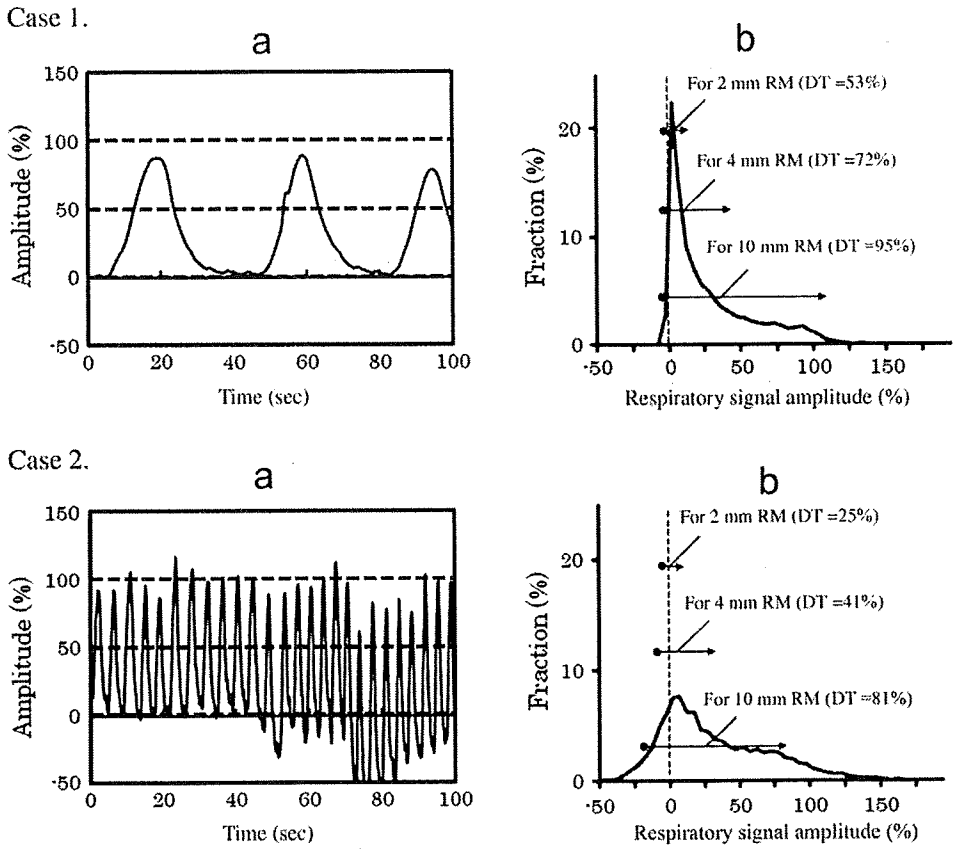

Fig. 4. Representative plots of 2 patients, 2 with no baseline drift (Case 1) and 1 with drift (Case 2). (a), representative plot of the patient's respiratory trace for a portion of a treatment. (b), histogram showing the variation in signal amplitude over an entire treatment.

Second, our study used more patients than have previous reports on respiratory motion. Adaptive treatment should be evaluated in terms of the efficiency with which patient variation can be managed. Therefore, more study participants, including greater variation, can demonstrate the efficiency of adaptation more clearly. There have been several reports of variations in respiratory motion for abdominal tumors for 4–24 patients (27, 28, 33). Equally, the management of respiratory data in these patients has been insufficient. The 42 patients in our study, who were assessed with highly sophisticated methods for evaluating tumor motion, provide more reliable data for application to the general population.

Third, we adopted amplitude-based respiratory gated radiation therapy for this simulation rather than the prevailing phase-based gating technique. Several reports have shown baseline drifting and irregular shape of respiratory signals, causing uncertainty in gating timing or tumor position when phase-based gating technique is introduced (27, 34). By contrast, amplitude-based gating is thought to be affected only marginally by variations in respiratory signal.

The patients in the current study showed respiration-induced tumor motion that ranged from 3 to 50 mm. The observed variation in respiration-induced tumor motion in this study suggests that a standardized window width is not adequate in clinical practice to achieve acceptable residual motion. When the standardized respiratory gating window width, which is the averaged window width for predefined

Table 3. Duty time for individualized respiratory gating window width and population-based window width

Residual motion (mm)	Duty time (%) Individualized window width	Population-based window width	*P* value
2	27.0 (4.4–78.9)	20.7 (5.3–42.4)	0.012
4	40.2 (11.4–97.3)	35.5 (16.5–58.3)	0.003
10	64.0 (32.2–99.1)	61.6 (39.9–81.5)	0.150

Both simulations were performed with a window level of 0%.

Table 4. Duty times for applied level

Residual motion (mm)	Duty time (%) IW-MEL	IF-MEL	P-MEL	L 0%
2	27.7	26.6	25.1	27.0
4	43.5	42.4	41.7	40.2
10	67.9	67.6	66.3	64.0

Abbreviations: IW-MEL = individualized maximum efficient level for whole session; IF-MEL = individualized maximum efficient level for first 10 breathing cycles; P-MEL = population-based maximum efficient level for whole session; L 0% = level of 0%;

Table 5. Duty times for applied level

	p value				
Residual motion (mm)	IW-MEL vs. L 0%	IF-MEL vs. L 0%	P-ME Lvs. L 0%	IW-MEL vs. P-MEL	IF-MEL vs. P-MEL
2	0.337	0.399	0.107	<0.001	0.006
4	<0.001	<0.001	0.009	<0.001	0.074
10	0.001	<0.001	0.049	0.061	0.054

Abbreviations: IW-MEL = individualized maximum efficient level for whole session; IF-MEL = individualized maximum efficient level for first 10 breathing cycles; P-MEL = population-based maximum efficient level for whole session; L 0% = level of 0%.

residual motion, was applied, half of the patients showed residual motion larger than predefined values. Furthermore, the remaining patients needed longer treatment times as a result of the inadequate window width. The current study shows that an individualized window width allows limitation of the residual motion to the predefined value. The duty times for gated radiation therapy with individualized window widths were significantly shorter than those with population-based window width.

The phenomenon is thought to result from uneven distribution of respiratory signal histograms. In this skewed distribution, window width extension to less frequent areas does not extend the duty time efficiently, and narrowing the width at areas of frequency loses duty time rapidly. Therefore, widths too great and those too narrow for the tumors both resulted in inefficient delivery when the generalized window width was applied.

To establish the most efficient window settings for respiratory gated radiation therapy, we explored the contribution of the window level to the duty time for each patient. Our results demonstrate that the most efficient levels were, on average, lower than the 0% level determined as that at the end of exhalation in early breathing cycles. Histogram analysis showed that the shift in the most efficient level from 0% could be attributed to baseline drift.

The adoption of both individualized and mean MELs increased the duty times compared with those using a 0% window level. Duty times for individualized MELs were significantly longer than those for mean MELs. However, the use of individualized MELs introduces a different practical problem. The respiratory gating window level should be set before treatment and should be fixed throughout the treatment session. Therefore, individual MELs for patients should be calculated in advance. We evaluated MELs on the first 10 breathing cycles to apply the setting to the following treatment sessions. However, the duty time for the MEL was not longer than the time for mean MEL. Therefore, the mean MEL, rather than the 0% level, should be introduced until the establishment of a more effective method of predicting an efficient level for each patient.

We measured abdominal wall motion as external respiratory signals. Several authors have argued discrepancies between the external respiratory signal and actual tumor position (27, 28). Tumor position corresponding to amplitude of external respiratory signal was determined by regression formula with fluoroscopy image and the respiratory signal. The respiratory signals used for the formula ranged from 0% to 100%. The current study revealed that window levels lower than 0% (−0.6% to −5.9%) allowed beams to be delivered most efficiently. In most cases, the MEL marginally out of range does not seem to cause significant deviation from the position calculated by the formula. However, other cases with relatively lower MEL reflecting large baseline drift are likely to need different parameters or different methods of applying the gating technique.

CONCLUSION

This study has demonstrated that variations in tumor track and patterns of respiration affect the reliable and efficient delivery of irradiation to liver tumors. Therefore, adapting respiratory gated radiation therapy for each patient is crucial. Individualized window widths, based on the preliminary evaluation of tumor tracks and the tolerable residual motion, can provide more precise and efficient treatment, and individualized window levels can also improve efficiency. However, methods for predicting the most efficient window level before the treatment require further investigation.

REFERENCES

1. Kawashima M, Furuse J, Nishio T, *et al.* Phase II study of radiotherapy employing proton beam for hepatocellular carcinoma. *J Clin Oncol* 2005;23:1839–1846.
2. Hashimoto T, Tokuuye K, Fukumitsu N, *et al.* Repeated proton beam therapy for hepatocellular carcinoma. *Int J Radiat Oncol Biol Phys* 2006;65:196–202.
3. Bush DA, Slater JD, Shin BB, *et al.* Hypofractionated proton beam radiotherapy for stage I lung cancer. *Chest* 2004;126:1198–1203.
4. Chiba T, Tokuuye K, Matsuzaki Y, *et al.* Proton beam therapy for hepatocellular carcinoma: a retrospective review of 162 patients. *Clin Cancer Res* 2005;11:3799–3805.
5. Wurm RE, Gum F, Erbel S, *et al.* Image guided respiratory gated hypofractionated stereotactic body radiation therapy (H-SBRT) for liver and lung tumors: Initial experience. *Acta Oncol* 2006;45:881–889.
6. Wada H, Takai Y, Nemoto K, *et al.* Univariate analysis of factors correlated with tumor control probability of three-dimensional conformal hypofractionated high-dose radiotherapy for small pulmonary or hepatic tumors. *Int J Radiat Oncol Biol Phys* 2004;58:1114–1120.
7. Seong J, Park HC, Han KH, *et al.* Clinical results and prognostic factors in radiotherapy for unresectable hepatocellular

carcinoma: A retrospective study of 158 patients. *Int J Radiat Oncol Biol Phys* 2003;55:329–336.
8. Park HC, Seong J, Han KH, *et al.* Dose-response relationship in local radiotherapy for hepatocellular carcinoma. *Int J Radiat Oncol Biol Phys* 2002;54:150–155.
9. Park W, Lim do H, Paik SW, *et al.* Local radiotherapy for patients with unresectable hepatocellular carcinoma. *Int J Radiat Oncol Biol Phys* 2005;61:1143–1150.
10. Dawson LA, Normolle D, Balter JM, *et al.* Analysis of radiation-induced liver disease using the Lyman NTCP model. *Int J Radiat Oncol Biol Phys* 2002;53:810–821.
11. Dawson LA, Ten Haken RK. Partial volume tolerance of the liver to radiation. *Semin Radiat Oncol* 2005;15:279–283.
12. Kato H, Tsujii H, Miyamoto T, *et al.* Results of the first prospective study of carbon ion radiotherapy for hepatocellular carcinoma with liver cirrhosis. *Int J Radiat Oncol Biol Phys* 2004; 59:1468–1476.
13. Suramo I, Paivansalo M, Myllyla V. Cranio-caudal movements of the liver, pancreas and kidneys in respiration. *Acta Radiol Diagn (Stockh)* 1984;25:129–131.
14. Shirato H, Seppenwoolde Y, Kitamura K, *et al.* Intrafractional tumor motion: lung and liver. *Semin Radiat Oncol* 2004;14: 10–18.
15. Kitamura K, Shirato H, Seppenwoolde Y, *et al.* Tumor location, cirrhosis, and surgical history contribute to tumor movement in the liver, as measured during stereotactic irradiation using a real-time tumor-tracking radiotherapy system. *Int J Radiat Oncol Biol Phys* 2003;56:221–228.
16. Keall PJ, Mageras GS, Balter JM, *et al.* The management of respiratory motion in radiation oncology report of AAPM Task Group 76. *Med Phys* 2006;33:3874–3900.
17. Brandner ED, Wu A, Chen H, *et al.* Abdominal organ motion measured using 4D CT. *Int J Radiat Oncol Biol Phys* 2006; 65:554–560.
18. Berson AM, Emery R, Rodriguez L, *et al.* Clinical experience using respiratory gated radiation therapy: comparison of free-breathing and breath-hold techniques. *Int J Radiat Oncol Biol Phys* 2004;60:419–426.
19. Underberg RW, van Sornsen de Koste JR, Lagerwaard FJ, *et al.* A dosimetric analysis of respiration-gated radiotherapy in patients with stage III lung cancer. *Radiat Oncol* 2006;1:8.
20. George R, Chung TD, Vedam SS, *et al.* Audio-visual biofeedback for respiratory-gated radiotherapy: impact of audio instruction and audio-visual biofeedback on respiratory-gated radiotherapy. *Int J Radiat Oncol Biol Phys* 2006;65: 924–933.
21. Berbeco RI, Nishioka S, Shirato H, *et al.* Residual motion of lung tumors in end-of-inhale respiratory gated radiotherapy based on external surrogates. *Med Phys* 2006;33:4149–4156.
22. Ohara K, Okumura T, Akisada M, *et al.* Irradiation synchronized with respiration gate. *Int J Radiat Oncol Biol Phys* 1989;17:853–857.
23. Mageras GS, Yorke E. Deep inspiration breath hold and respiratory gating strategies for reducing organ motion in radiation treatment. *Semin Radiat Oncol* 2004;14:65–75.
24. Balter JM, Brock KK, Litzenberg DW, *et al.* Daily targeting of intrahepatic tumors for radiotherapy. *Int J Radiat Oncol Biol Phys* 2002;52:266–271.
25. Hoisak JD, Sixel KE, Tirona R, *et al.* Correlation of lung tumor motion with external surrogate indicators of respiration. *Int J Radiat Oncol Biol Phys* 2004;60:1298–1306.
26. Hoisak JD, Sixel KE, Tirona R, *et al.* Prediction of lung tumour position based on spirometry and on abdominal displacement: accuracy and reproducibility. *Radiother Oncol* 2006;78: 339–346.
27. Sharp GC, Lu HM, Trofimov A, *et al.* Assessing residual motion for gated proton-beam radiotherapy. *J Radiat Res (Tokyo)* 2007;48(Suppl A):A55–A59.
28. Berbeco RI, Nishioka S, Shirato H, *et al.* Residual motion of lung tumours in gated radiotherapy with external respiratory surrogates. *Phys Med Biol* 2005;50:3655–3667.
29. Vedam SS, Keall PJ, Kini VR, *et al.* Determining parameters for respiration-gated radiotherapy. *Med Phys* 2001;28:2139–2146.
30. Minohara S, Kanai T, Endo M, *et al.* Respiratory gated irradiation system for heavy-ion radiotherapy. *Int J Radiat Oncol Biol Phys* 2000;47:1097–1103.
31. Shirato H, Oita M, Fujita K, *et al.* Three-dimensional conformal setup (3D-CSU) of patients using the coordinate system provided by three internal fiducial markers and two orthogonal diagnostic X-ray systems in the treatment room. *Int J Radiat Oncol Biol Phys* 2004;60:607–612.
32. Seppenwoolde Y, Shirato H, Kitamura K, *et al.* Precise and real-time measurement of 3D tumor motion in lung due to breathing and heartbeat, measured during radiotherapy. *Int J Radiat Oncol Biol Phys* 2002;53:822–834.
33. George R, Ramakrishnan V, Siebers JV, *et al.* Investigation of patient, tumour and treatment variables affecting residual motion for respiratory-gated radiotherapy. *Phys Med Biol* 2006;51:5305–5319.
34. Ford EC, Mageras GS, Yorke E, *et al.* Evaluation of respiratory movement during gated radiotherapy using film and electronic portal imaging. *Int J Radiat Oncol Biol Phys* 2002;52:522–531.

● 特 集 ● 陽子線治療の現状と限界

静岡がんセンターの陽子線治療

村山 重行　藤　浩*

〔*Jpn J Cancer Chemother* 36(11): 1806-1812, *November*, 2009〕

Proton Beam Therapy at Shizuoka Cancer Center: Shigeyuki Murayama and Hiroshi Fuji (*Proton Therapy Division, Shizuoka Cancer Center*)

Summary

Proton beam therapy (PBT) is a type of radiation therapy using positively-charged particles, i. e. protons, for the treatment of malignant tumor, and is also an advanced high-technology radiotherapy using large-scale equipment, such as a synchrotron accelerator or isocentric rotational gantry systems. Since a proton beam has advantageous physical properties, i. e. Bragg peak peculiar to a charged particle beam, in formation of dose distribution as compared with megavoltage x-rays in a conventional radiotherapy, a delivery of a conformal high dose to a localized target volume is easily attained, and both improvement in local control rate and reduction of normal tissue impairment can be expected as the result. PBT is adopted mainly as a radical treatment for patients with early-stage or locally-advanced prostatic cancer, hepatocellular carcinoma, non-small cell lung cancer, or head & neck malignant tumor. Moreover, the benefits of PBT may be shared not only with a pediatric patient who is easily injured and growth disturbed by even low-level irradiation of normal tissues/organs and also with an inoperable elderly patient with several medical complications. Insurance coverage in connection with its use for certain diseases is recently under discussion. This paper describes the actual status of PBT including present activities and clinical experiences at Shizuoka Cancer Center about 5 years from the start of PBT. **Key words**: Proton beam therapy, Neoplasms, Charged particle therapy, **Corresponding author**: Shigeyuki Murayama, Proton Therapy Division, Shizuoka Cancer Center, 1007 Shimonagakubo, Nagaizumi-cho, Suntou-gun, Shizuoka 411-8777, Japan

要旨　陽子線治療は荷電粒子線による悪性腫瘍に対する放射線治療の一つであり，シンクロトロン加速器や回転ガントリー照射システムなど大規模な装置を利用する先進医療である。陽子線は通常の放射線治療で利用する高エネルギーX線と比較して，線量分布の形成において有利な物理特性，すなわち荷電粒子線に特有のブラッグピークをもつので，限局した標的体積への均一な高線量の投与が容易に可能であり，その結果として局所制御率の向上と正常組織障害の低減が期待される。陽子線治療の主な適応は前立腺癌・肝癌・非小細胞肺癌・頭頸部悪性腫瘍の早期症例または局所進行症例に対する根治治療である。さらに正常組織・器官への低レベルの放射線によっても，成長障害などの影響を受けやすい小児腫瘍や合併症を有する手術不能な高齢者症例にも陽子線治療のベネフィットがあると考えられる。現在，一部の疾患に対する保険収載が検討されている。本稿では静岡がんセンターにおいて開始から約5年を経た陽子線治療の経験を含め，陽子線治療の現状を述べる。

はじめに

高齢者や他の根治治療が困難な合併症をもつ患者に対するQOL (quality of life) を重視したがん治療への関心が高まるなかで，それら症例に対しても安全に適応可能な高精度放射線治療法の重要性が増している。

放射線治療における根治照射では，腫瘍周囲の正常組織の耐容線量により規定される投与可能最大線量が，腫瘍制御線量に達しなければ治療は成立しない。放射線腫瘍医はコンピュータ化された線量分布出力が容易に得られるようになる以前から，常に腫瘍への線量をいかに集中させるかに腐心し，そのための方法論を関連領域の企業や技術者とともに開発してきた。子宮頸癌や頭頸部癌で確立された密封小線源治療法はその代表例であり，粒子線治療（陽子線治療・重粒子線治療）は今日その同じ目標に向けて研究を続けている。

* 静岡県立静岡がんセンター・陽子線治療科

連絡先: 〒411-8777 静岡県駿東郡長泉町下長窪1007　静岡県立静岡がんセンター・陽子線治療科
村山　重行

表1　国内外の陽子線治療施設と患者数

	施設数	施設名・所在地	治療開始年	治療患者数[注1]	備考
日本	6	国立がんセンター東病院（柏市）	1998	607	Gantry（+）[注2]
		兵庫県立粒子線医療センター（たつの市）	2001	2,033	Gantry（+）
		筑波大学陽子線医学利用研究センター（つくば市）	2001	1,367	Gantry（+），他に旧施設（1983～2000）で700例
		若狭湾エネルギー研究センター（敦賀市）	2002	56	
		静岡県立静岡がんセンター（静岡県駿東郡長泉町）	2003	692	Gantry（+）
		南東北がん陽子線治療センター（郡山市）	2008	50	Gantry（+）
		（参考：放射線医学総合研究所（千葉市）	1979	145	2002年に終了）
アメリカ	6	Massachusette General Hospital (MGH)/ボストン	2001	3,515	Gantry（+），他に旧施設（1961～2002）で9,116例
		Loma Linda Univ Medical Center (LLUMC)/カリフォルニア	1990	13,500	Gantry（+）
		Mideast Proton Radiotherapy Institute (MPRI)/インディアナ	2004	632	Gantry（+），他に旧施設（1993～1999）で34例
		UCSF-UC Davis/カリフォルニア	1994	1,113	眼治療のみ
		Florida Proton Therapy Institute (FPTI)/フロリダ	2006	988	Gantry（+）
		MD Anderson Cancer Center (MDACC)/ヒューストン	2006	1,000	Gantry（+）
ロシア[注1]	3	ITEP/モスクワ	1969	4,024	
		サンクトペテルブルグ	1975	1,327	
		ドゥブナ	1999	402	他に旧施設（1967～1996）で124例
フランス	2	ニース	1991	3,690	
		ICPO/オルセイ/パリ	1991	4,497	うち眼治療は3,676例
スイス	1	Paul Scherrer Institut（PSI)/フィリゲン	1984	5,076	72 MeV眼治療専用装置
			1996	426	Gantry（+），230 MeV
スウェーデン	1	ウプサラ	1989	929	他に旧施設（1957～1976）で73例
英国	1	クラッタブリッジ	1989	1,803	眼治療のみ
南アフリカ	1	iThemba Labs/ファウレ	1993	503	
カナダ	1	TRIUMF/バンクーバー	1995	137	眼治療のみ
ドイツ	1	Hahn-Meitner-Institut（HMI)/ベルリン	1998	1,227	眼治療のみ
イタリア[注1]	1	INFN-LNS/カタニア	2002	151	眼治療のみ
中国	1	Wanjie Proton Therapy Center/山東省	2004	767	Gantry（+）
韓国	1	National Cancer Center（NCC)/ソウル	2007	330	Gantry（+）
				50,987	終了施設を含む治療患者総数は約61,000例

出典：PTCOG web site（http://ptcog.web.psi.ch/ptcentres.html）から一部改変
[注1]：患者数は2008年12月末現在の報告数（ただしロシア，イタリアは2007年末現在）
[注2]：Gantry（+）：回転ガントリー照射室をもつ施設

Ⅰ．陽子線治療の歴史と治療施設の現状

1．陽子線治療の歴史

陽子線を用いるがん放射線治療の研究は1950年代に米国とスウェーデンで始まり，わが国の放射線医学総合研究所と筑波大学の施設を含む高エネルギー加速器が利用可能な研究所などにおいて，照射技術の開発と臨床的検討が行われた。初期には進行乳癌患者に対する下垂体照射，低エネルギー陽子線による脈絡膜メラノーマの眼球保存治療や頭蓋底腫瘍に対する非手術的治療としての有用性が研究され，欧米のいくつかの施設は現在も眼腫瘍治療のみを実施している。粒子線治療の先駆けは1930年代に始まった速中性子線による高LET放射線治療である。しかし，飛程調節とピーク拡大により実現される線量分布において勝る荷電粒子線，すなわち陽子線や重粒子線に代表の座を譲った[1]。

2．陽子線治療施設の現状

現在稼動中の陽子線治療施設，国別施設数，2008年末までの治療患者概数を表1に示す。国内に6か所，国外では米国を中心に20か所の施設が稼働中で，エネルギーが230 MeV以上で深部病巣まで到達可能な陽子線を利用できる施設のほとんどが回転ガントリー照射室を有し